Complete characterization by Raman spectroscopy of the structural properties of thin hydrogenated diamond-like carbon films exposed to rapid thermal annealing

Franck Rose, Na Wang, Robert Smith, Qi-Fan Xiao, Hiroshi Inaba, Toru Matsumura, Yoko Saito, Hiroyuki Matsumoto, Qing Dai, Bruno Marchon, Filippo Mangolini, and Robert W. Carpick

---

Articles you may be interested in

The local crystallization in nanoscale diamond-like carbon films during annealing
Appl. Phys. Lett. 105, 233110 (2014); 10.1063/1.4903803

Gold nanoparticle formation in diamond-like carbon using two different methods: Gold ion implantation and co-deposition of gold and carbon
J. Appl. Phys. 112, 074312 (2012); 10.1063/1.4757029

Superhard behaviour, low residual stress, and unique structure in diamond-like carbon films by simple bilayer approach
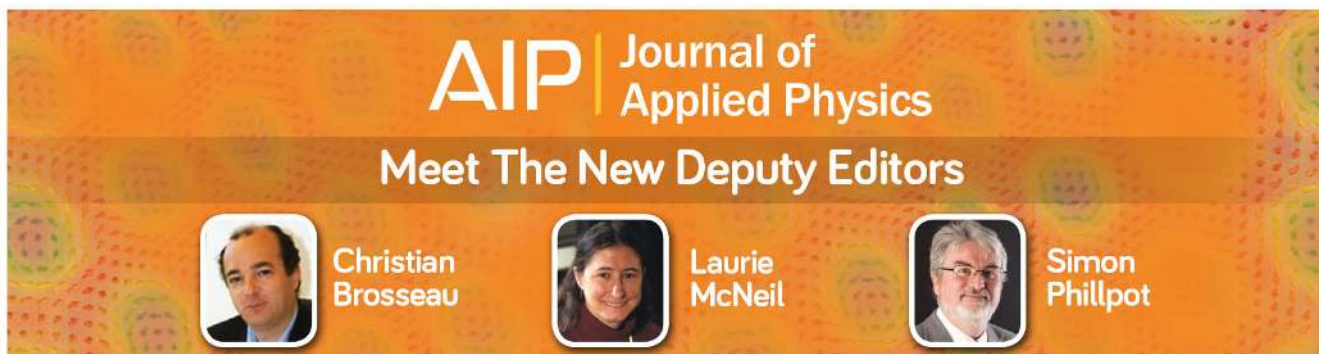J. Appl. Phys. 112, 023518 (2012); 10.1063/1.4739287

Deposition of diamond-like carbon film on phase-change optical disk by PECVD
J. Vac. Sci. Technol. B 23, 24 (2005); 10.1116/1.1835274

Deposition of hydrogenated diamond-like carbon films under the impact of energetic hydrocarbon ions
J. Appl. Phys. 84, 5538 (1998); 10.1063/1.368599

Complete characterization by Raman spectroscopy of the structural properties of thin hydrogenated diamond-like carbon films exposed to rapid thermal annealing

Franck Rose,[1,a)] Na Wang,[1] Robert Smith,[1] Qi-Fan Xiao,[1] Hiroshi Inaba,[2] Toru Matsumura,[2] Yoko Saito,[2] Hiroyuki Matsumoto,[2] Qing Dai,[1] Bruno Marchon,[1] Filippo Mangolini,[3] and Robert W. Carpick[4]

[1]*HGST, A Western Digital Company, San Jose Research Center, 3403, Yerba Buena Rd, San Jose, California 95135, USA*
[2]*HGST, A Western Digital Company, Japan Research Laboratory, 2880 Kozu, Odawara, Kanagawa 256-8510, Japan*
[3]*Department of Materials Science and Engineering, University of Pennsylvania, Philadelphia, Pennsylvania 19104, USA*
[4]*Department of Mechanical Engineering and Applied Mechanics, University of Pennsylvania, Philadelphia, Pennsylvania 19104-6315, USA*

We have demonstrated that multi-wavelength Raman and photoluminescence spectroscopies are sufficient to completely characterize the structural properties of ultra-thin hydrogenated diamond-like carbon (DLC:H) films subjected to rapid thermal annealing (RTA, 1 s up to 659 °C) and to resolve the structural differences between films grown by plasma-enhanced chemical vapor deposition, facing target sputtering and filtered cathodic vacuum arc with minute variations in values of mass density, hydrogen content, and sp^3 fraction. In order to distinguish unequivocally between films prepared with different density, thickness, and RTA treatment, a new method for analysis of Raman spectra was invented. This newly developed analysis method consisted of plotting the position of the Raman G band of carbon versus its full width at half maximum. Moreover, we studied the passivation of non-radiative recombination centers during RTA by performing measurements of the increase in photoluminescence in conjunction with the analysis of DLC:H networks simulated by molecular dynamics. The results show that dangling bond passivation is primarily a consequence of thermally-induced sp^2 clustering rather than hydrogen diffusion in the film. © *2014 AIP Publishing LLC*. [http://dx.doi.org/10.1063/1.4896838]

I. INTRODUCTION

Hydrogenated diamond-like carbon[1–4] (DLC:H) films are lynchpin materials in today's hard disk drives (HDDs) since they protect both magnetic discs and recording heads from corrosion and wear.[5–10] To achieve high capacity storage with high areal densities on the order of 1 Tb/in.[2], the distance between the magnetic sensors in the heads and the magnetic media on the disks, which is typically around 80 to 100 Å, has to be reduced to around 65 to 89 Å.[11,12] Consequently, the thickness of the protective DLC:H films which is the main contributor to the spacing needs to decrease from its typical value of 20 to 30 Å today to only 20 to 25 Å.[11,12]

Since these films are employed to fulfill different functions on the disks, such as providing a barrier against corrosion, planarization, durability, and protection against contamination, it is of technological and scientific interest to understand whether ultra-thin DLC:H films (thickness below 50 Å) can retain the well-characterized physical properties, composition and microstructure of thicker films (thickness around 200 Å) and whether they have a non-uniform cross-sectional structure. For instance, it is known that carbon films[13–18] can exhibit different fractions of sp^2 and sp^3 bonded carbon in the surface top-most layer compared to the deeper layers. Thus, understanding whether cross-sectional non-uniformity can impact film performance in HDD is of primary importance. Moreover, in future heat-assisted magnetic recording (HAMR)[19–22] HDDs operating at 1 Tb/in.[2], the DLC:H protection coatings on the disks and heads will need to remain thermally stable.[23–28] In HAMR, an anisotropic magnetic material such as FePt with L1$_0$ phase is used as the recording medium on the disk. This magnetic medium is heated above its Curie temperature between 450 °C and 650 °C using a near-field plasmonic antenna on the head. The heat temporarily lowers the medium's coercivity and enables writing. During this process, the protective DLC:H film, which is deposited directly on the magnetic medium, will experience elevated temperatures as well. Hence, studying the kinetics of the thermally induced structural evolution of ultra-thin DLC:H is also of primordial technological and scientific interest.[1,29–44]

To apply HAMR technology in future HDDs, engineers and researchers must determine whether DLC:H films can still be used as protective overcoats at reduced thicknesses in high temperature conditions or whether they should be replaced with more robust alternative materials. In order to answer all these challenging scientific and technical questions about carbon overcoats, one has to be able to describe

a)Author to whom correspondence should be addressed. Electronic mail: franck.rose@hgst.com. Tel.: (408)-717-5798. Fax: (408)-717-9073.

the complex microstructure of these ultra-thin films and to measure their properties. One difficulty with real HAMR laser heating is that the affected area only covers a few magnetic grains, which is beyond the spatial resolution of most of the available characterization techniques, if not all of them. An alternative heating technique should be used instead of a near-field laser. Rapid thermal annealing (RTA) utilizes two densely-packed rows of tungsten-halogen lamps to heat up samples at a rate of $\sim 100\,^\circ$C/s, which is among the fastest in conventional annealing techniques. However, the ramp-up rate is still significantly slower compared to the laser heating ($\sim 10^{11}\,^\circ$C/s) utilized in HAMR application. Nevertheless, the total heating time of a given spot on the disk during a mean HAMR hard-disk lifetime is estimated to be on the order of seconds, which is comparable to the RTA experimental time scale. Therefore, RTA could be considered as an alternative experimental method to examine the carbon overcoat structural integrity at elevated temperatures.

The atomic network of DLC:H films can be seen as a complex arrangement of disordered hydrogen-terminated carbon nanostructures comprised locally of tetrahedral carbon, delocalized six-fold aromatic rings, non-delocalized rings and polymeric chains containing deformed bonds with a distribution of lengths, orientations, and angles.[1] Indeed, the microstructure of DLC:H films is often described as a complex amorphous matrix consisting of highly disordered sp^2-bonded carbon nanoclusters linked together by sp^3-bonded carbon atoms[1] where hydrogen atoms terminate dangling bonds. This description of the DLC:H network where sp^2 clusters are embedded in a sp^3 bonded matrix is often called the Robertson model.[1] Even though it is a well-accepted model for amorphous carbon network, the limitation of experimental techniques makes it nearly impossible to further prove the validity of this model. In DLC:H, the lack of crystallinity inhibits the use of any diffraction techniques and renders structural characterization an extremely challenging materials science problem. Consequently, any structural model that describes DLC:H is difficult to prove. Fortunately, molecular dynamics (MD)[45–48] provides some insights into the microstructure of amorphous carbon from an atomic perspective and enables the interpretation of results in a statistical way.

Due to the complexity of the microstructure, different thermally induced processes can occur with different activation energies at different carbon sites in the amorphous network.[1,29–44] For such films created by plasma-enhanced chemical vapor deposition of acetylene (PECVD) and used in HDDs, Mangolini *et al.*[41] showed that under slow annealing in high vacuum three different thermally induced processes occur at different carbon sites of the DLC:H network with an assumed Gaussian distribution of activation energies E and standard deviation σ, namely: (a) clustering of the carbon sp^2 phase with $E = 0.18$ and $\sigma = 0.05$ eV, (b) scission of the sp^3-hybridized C-H bond with $E = 1.7$ and $\sigma = 0.5$ eV (concomitant hydrogen diffusion in the film can promote more sp^2-bonding and clustering) and c) direct conversion of sp^3- into sp^2-bonded carbon with $E = 3.5$ and $\sigma = 0.5$ eV.

The mass density ρ and the total C-C+C-H sp^3-bonded carbon fraction f_{sp3} of DLC:H films used in HDDs are

commonly adopted as benchmarks to assess their potential performance as protective overcoats. The general usage is to consider that a higher sp^3 fraction is translated into higher density which allows reduction of the overcoat thickness for equal or better protection performance (i.e., the denser the film the better it forms an anticorrosion protection barrier). Direct measurement of the sp^3 content and mass density of ultra-thin films and their evolution under thermal annealing is an experimental challenge that can lead to improper use or interpretation of spectroscopic techniques, especially X-ray photoelectron spectroscopy (XPS) and visible resonant Raman spectroscopy. For instance, attempting to measure a chemical shift between sp^2 and sp^3 components fitted in the C1s spectra of XPS is an improper but still widely used method.[41,49–51] Another example is the misinterpretation of the ratio between the first order Raman D and G bands of carbon as the sp^2 to sp^3 ratio.[35] In the case of mass density measurements, which are carried out by using X-ray Reflectivity (XRR), the experimental difficulty lies in the evaluation of the density of the ultra-thin films.[52,53] Since XRR cannot be used to measure density on films thinner than 200 Å thick, one has to guess or use extrapolation to determine whether ultra-thin films retain the density of thicker films.

The objective of the present paper is to demonstrate that it is possible to completely characterize the structural properties of as-deposited and post-annealed DLC:H films and to resolve the structural differences between different types of films by using multi-wavelength (MW) Raman spectroscopy[35,54–68] and photoluminescence (PL) spectroscopy.[38–40,69–73] During data analysis, the key to achieve a complete and comprehensive structural characterization is (a) to take account of both the structural and topological disorder of the amorphous network, (b) be aware that the evolution of the sp^2 and sp^3 phases can in principle be independent, (c) that this evolution depends on the treatment of the film post-deposition, and finally (d) that sp^2 clusters possess locally different band gaps that are more or less resonant with different Raman laser wavelengths.

By correct interpretation of the different parameters derived from the spectral analysis from curve fitting of MW Raman[35,54–68] and PL[38–40,69–73] spectra, we report that it is possible to distinguish between DLC:H films with minute differences in bonding configuration, microstructure, and hydrogen content and to follow their thermally induced structural evolution. Most importantly, we introduce a new analysis method of Raman spectra that permits distinguishing between films prepared with different density, thickness, and RTA treatment. This method consists of plotting the variation of the position Pos(G) of the Raman G band of carbon versus its full width at half maximum FWHM(G). Pos(G) is a measure of the topological disorder (size and shapes of sp^2 clusters) and FWHM is a measure of the structural disorder (bond lengths and angles in sp^2 clusters). We show that this method is sufficient to completely characterize the structural properties of the films.

We also demonstrate that the model by Mangolini *et al.*[41] still applies to shorter time scales (1s RTA) and that thermally induced hydrogen diffusion and sp^2 clustering in the film can both lead to dangling bonds passivation. This

passivation of non-radiative recombination centers is measured by an increase in PL background signal.

Finally, MD has been utilized to simulate the thermal annealing process of a hydrogenated amorphous carbon film built by atom-by-atom deposition. The temperature effects and the reconstruction of the carbon network will be discussed.

II. EXPERIMENTAL SET-UP

Five types of films with different values of mass density ρ, hydrogen content f_H, and total C-C+C-H sp^3-bonded carbon content f_{sp3} were investigated under 1s RTA[29] up to 659 °C in dry air (under constant flows of 8000 sccm of N_2 and 2000 sccm of O_2, and relative humidity below 5%). These different values of ρ, f_H, and f_{sp3} (Table I) were obtained by utilizing different deposition methods, namely PECVD of acetylene (NCT source by Intevac Inc, with acceleration bias of ions of 60, 120, and 180 V), facing target sputtering (FTS, CDPS source by Intevac Inc), and filtered cathodic vacuum arc (FCVA, Nanofilm Technologies International).

All DLC:H films (thicknesses 25 to 200 Å) were deposited onto a 1000 Å NiTa-coated glass disks. Their thicknesses and mass densities were measured by XRR (PANalytical X'Pert PRO).

Raman spectra were obtained using a Renishaw In Via confocal Raman microscope equipped with four laser wavelengths λ_L of 244 nm (ultra-violet (UV)), 488 and 514 nm (visible blue and green), and 830 nm (near infra-red (nIR)). PL was acquired at 488 nm by replacing the Rayleigh rejection filter by a PL filter. For all wavelengths, the laser spot was transformed into a line in order to prevent film degradation, and the laser power on the disk was maintained below 1 mW. In order to reduce laser irradiation in the particular case of UV Raman, disks were translated by 1 μm in the radial direction every millisecond while rotating at 5400 rpm.

The spectral analysis of first order Raman data was obtained by Gaussian deconvolution into D and G bands. Prior to curve fitting, the instrument background measured on a reflecting film (disk coated with 1000 Å of NiTa) was subtracted and the noise removed by applying a Butterworth low pass filter.[74] The PL background signal was deconvoluted using the asymmetric least squares smoothing method[75] and then subtracted from the spectrum. Finally, Gaussian fitting

was carried out using the non-linear least squares method using the Levenberg-Marquardt algorithm.[76,77]

In the 514 nm case, the slope S of the deconvoluted PL background signal under the first order Raman spectrum (wavenumbers between 900 and 1900 cm^{-1}) was determined by a linear fit. The evolution of the hydrogen content f_H, diffusion, and bonding (i.e., passivation of the dangling bonds) was monitored using PL spectroscopy (ratio of the PL slope to G band intensity S/I(G)[69]) in conjunction with Hydrogen Forward Scattering (HFS, Evans Analytical Group).

Small variations in sp^3-bonded carbon content f_{sp3} could be quantified by measuring the dispersion Disp(G) of the G band position with λ_L.[35,54–68] f_{sp3} values obtained by MW Raman on PECVD films were compared with measurements obtained by XPS and X-ray-induced Auger electron spectroscopy (XAES). A description of the XPS set-up and analysis is given in Mangolini *et al.*[41]

III. MOLECULAR DYNAMICS MODELING AND NUMERICAL EXPERIMENTS

A. Model of film deposition process

MD utilizes Newton's second law to simulate atomic trajectories where the interatomic forces are governed by an interaction potential. In this paper, the second generation reactive empirical bond order (REBO) potential,[78–81] which is one of the most widely used and acclaimed potentials for hydrocarbon related studies, is adopted. The equations of motion are integrated by the velocity-Verlet method with a time step of 0.5 fs as implemented in the large-scale atomic/molecular massively parallel simulator (LAMMPS[82]) code.

The simulated amorphous carbon film was generated by depositing carbon and hydrogen atoms one after another on a diamond substrate. The lateral positions of the incident carbon and hydrogen atoms were generated randomly in the *x-y* plane above the substrate at a distance of 55 Å from the bottom of the diamond substrate. To simulate the normal incidence at the diamond surface, each atom was assigned a velocity in the negative *z*-direction with a magnitude commensurate to the desired energy of 40 eV. During the simulation of the deposition process, the bottom three layers of atoms in the diamond (100) substrate were fixed to mimic a semi-infinite half-space. Atoms in the next four layers above the fixed atoms were coupled to an external heat bath

TABLE I. Mass density ρ (XRR), C-C+C-H sp^3 fraction f_{sp3} (MW Raman), hydrogen content f_H (HFS), and Gaussian fitting results (514 nm Raman spectra in Figs. 1(a) and 1(b)) of 200 Å thick DLC:H films prepared by PECVD (ion acceleration bias of 60, 120, and 180 V), FTS and FCVA before (30 °C) and after 1s RTA (659 °C).

	PECVD 60 V		PECVD 120 V		PECVD 180 V		FTS		FCVA	
1s RTA	30 °C	659 °C	30 °C	659 °C	30 °C	659 °C	30 °C	668 °C	30 °C	650 °C
ρ (g/cm^3)	1.82	1.76	2.05	2.04	2.14	2.10	2.56	2.56	3.09	3.09
f_{sp3} (%)	52.58	46.37	54.03	47.87	54.81	49.51	59.9	50.15	68.18	58.53
f_H (%)	32.5	24.7	32	27.5	30.5	28	5.8	5.5	<0.5	<0.5
Pos(G) (cm^{-1})	1531	1542.2	1538.9	1549.4	1542.2	1554.8	1559.5	1567.7	1565.9	1571
FWHM(G) (cm^{-1})	178.6	159.9	187.9	170.1	187.5	168.4	206.2	191.8	210.1	197.3
I(D)/I(G)	0.31	0.33	0.32	0.37	0.35	0.41	0.53	0.6	0.41	0.42
S/I(G) (μm)	3.64	8.25	1.61	3.2	0.98	1.63	0.32	0.37	0.28	0.5

through a Berendsen thermostat.[83] To minimize the effect of the thermostat on the deposition process, all substrate atoms within a cylinder centered on the impacting carbon atom were allowed to move freely, whereas all other remaining substrate atoms were connected to the thermostat.[46,84] With this technique, atoms coupled to the heat bath were time integrated during the deposition of each atom, and the effect of the thermostat on the interaction between deposited carbon atoms and substrate atoms was significantly reduced.

The system was allowed to relax for 2 ps between each atomic deposition and then to be equilibrated by the heat bath. The relaxation time was chosen based on Marks's study[85] which showed that the thermal spike lifetime was less than 0.5 ps for ion energy below 100 eV. Atoms sputtered off from the substrate were removed from the system before injecting the next atom. The complete system was then equilibrated at room temperature (RT) for 10 ps after the deposition. The final configuration was then used in the numerical rapid thermal annealing.

B. Numerical rapid thermal annealing process

The numerical annealing experiments were conducted with the DLC:H film generated with the MD atom deposition method described in the previous section. During thermal annealing, the temperature control of the model was divided into four groups. The bottom layer of atoms was fixed to simulate the semi-infinite half-space. The temperature of the atoms in the next five layers was fixed at RT by the Berendsen thermostat.[83] All of the other atoms in the substrate moved freely without any external constrains. Both of the carbon and hydrogen atoms in the amorphous film were controlled by a designated temperature profile. Four peak temperatures 317 °C, 570 °C, 745 °C, and 1135 °C were studied in this simulation. For each case, the temperature of the DLC:H film was ramped up to the peak temperature from RT in 10 ps. After holding at the peak temperature for 200 ps, a two-stage cooling model was applied to simulate the cooling process. The first cooling stage was a fast-cooling process, which reduced the temperature to 60% of the peak value. This stage was followed by a slow-cooling process, which gradually lowered the temperature below 177 °C. Finally, the whole system was equilibrated at RT. The carbon film changes were then characterized after the film reached equilibrium at RT.

C. Bond-order analysis

The bond order analysis of the DLC:H network was performed with Materials Studio Visualizer[86] which utilizes a distance-based criterion to calculate the existence of covalent bonds. The order of each bond was incrementally optimized based on the coordination number of nearest neighbor atoms. Each H atom was permitted to form only one covalent bond with bond order of one. Since electronically satisfied C atoms have a valence of 4, calculating the valence of each carbon atom as derived from bond order analysis enables us to quantify the number of dangling bonds in the film. We define the number of dangling bonds a C atom possesses as 4 minus the instantaneous C valence number, and this method

is used to calculate the dangling bond density after RTA treatment for each peak temperature.

IV. VISIBLE RAMAN AND PL SPECTROSCOPIES: sp² CLUSTERING

In order to resolve the structural differences between the films, we used resonant visible Raman spectroscopy which is the tool of choice to study carbon-based materials.[1,35,54–68,87–90] In graphite as well as in DLC:H, the π states are more polarizable and reside at lower energy than the σ states.[1] In the electronic band structure of DLC:H, the π states form the conduction and valence band edges and are responsible for the relatively small optical band gaps, typically in the range of 0.4 to 2.5 eV.[1] Therefore, at visible laser wavelengths, the Raman process is always resonant,[1] and the Raman cross section of π states is more than fifty times higher than that of σ states.[1] Consequently, the visible Raman spectra of DLC:H in Fig. 1 are dominated by carbon atoms in the sp² hybridization, and the bands' intensity, position, and width measured in these spectra (Figs. 2 and 3) reflect the clustering and disorder of the sp² sites. Visible Raman and PL spectra (Fig. 1) as well as the variation of f_{sp3} derived from fitting MW Raman spectra (Fig. 4) clearly reveal differences between films with different density and RTA treatment. The observed spectral features in Fig. 1 are the D and G bands with their overtones superimposed on a PL signal. The absence of translational symmetry in DLC:H relaxes the fundamental Raman selection rule (i.e., break down of wave vector conservation).[90] Therefore, in the first order scattering process (one phonon process), it is possible to access excitations away from the center of the Brillouin zone. This results first in the broadening of the Γ point zone center phonon, the G band, and second in the appearance of a K point longitudinal-optical phonon, the D band. The G band corresponds to the in-plane bond stretching motions of any pairs of sp² atoms. It occurs at all sp² sites, both in rings and chains, and possesses the E_{2g} symmetry.[1,54–68,87–90] The D band is a breathing mode of A_{1g} symmetry, and its intensity is strictly related to the occurrence of six-fold aromatic rings in the scattering medium.[1,54–68,77–90] Thomsen and Reich[91,92] have demonstrated that the appearance of the D band is defect-induced and involves a double resonant Raman scattering process. Figs. 1(a) and 1(b) display the first and second order Raman spectra obtained with $\lambda_L = 514$ nm and a Rayleigh rejection filter, and Figs. 1(c) and 1(d) give the first, second, and third order Raman spectra on top of the complete PL signal using $\lambda_L = 488$ nm and a PL filter. The results of Gaussian fitting of 514 nm Raman spectra are presented in Figs. 2 and 3.

The size of the sp² phase organized in six-fold aromatic rings in DLC:H can be measured by the intensity ratio I(D)/I(G) of the D and G bands[1] (Figs. 3(a) and 3(b)). If the sp² phase is predominantly comprised of chains, then the value of the I(D)/I(G) is close to zero.[1] Likewise, if rings are disordered, distorted or comprised of closed chains such that the bonds are not fully delocalized on the rings then I(D)/I(G) is also negligible.[1] Fig. 3(a) reveals that clustering of the sp² phase organized in rings is more important for thinner films
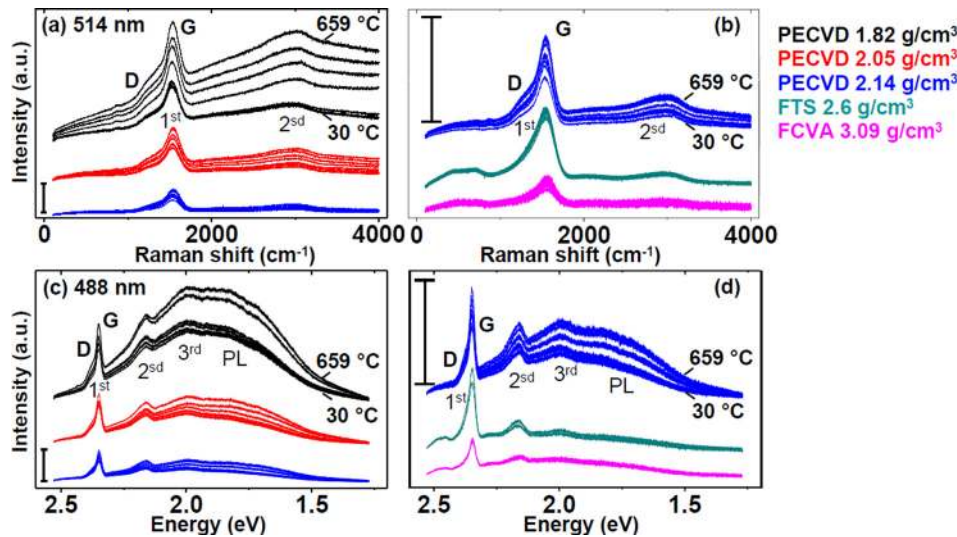
FIG. 1. (a) and (b) intensity of the 514 nm Raman spectra versus Raman shift in wavenumber and (c) and (d) intensity of the 488 nm PL spectra versus absolute energy in eV of the scattered light. All DLC:H films are 200 Å thick. The intensity scale bar and the spectra (blue) of PECVD 2.14 g/cm³ in (a) and (c) are reported and zoomed in (b) and (d), respectively. The first, second and third order of the D and G Raman bands are indicated. For each set of data (densities in g/cm³ from top to bottom: 1.82 (black), 2.05 (red) and 2.14 (blue) in (a) and (c), 2.14 (blue), 2.56 (cyan) and 3.09 (magenta) in (b) and (d)) the bottom spectrum corresponds to the as-deposited film at 30 C. The other spectra are those of the 1s RTA-treated films arranged (bottom to top) in the order of increasing temperature: 123, 244, 332, 396, 511, 553, 645, and 659 °C for PECVD, 200, 280, 346, 426, 442, 476, 555, 639, 668 °C for FTS, 150, 450, 600, 650 °C for FCVA.

as the ratio I(D)/I(G) decreases with thickness for all types of films. More precisely, in the PECVD and FTS cases, it can be noticed that I(D)/I(G) reaches a minimum or a plateau around 100 Å followed by slight increase in value at 200 Å. This increase can possibly be due to a slight increase in deposition temperature at longer deposition times. Moreover, we found that the values of the I(D)/I(G) ratio of the less dense

PECVD films are much lower than the values for FTS and FCVA films. This latter finding can be explained by the higher hydrogen content of PECVD films (around 32%, see Table I) which reduces aromatic ring formation.[1] Fig. 3(b) shows that all films have similar thermal evolution and exhibit a sharp increase of I(D)/I(G) over 450 °C. These results are well described by the Robertson model[1] which explains
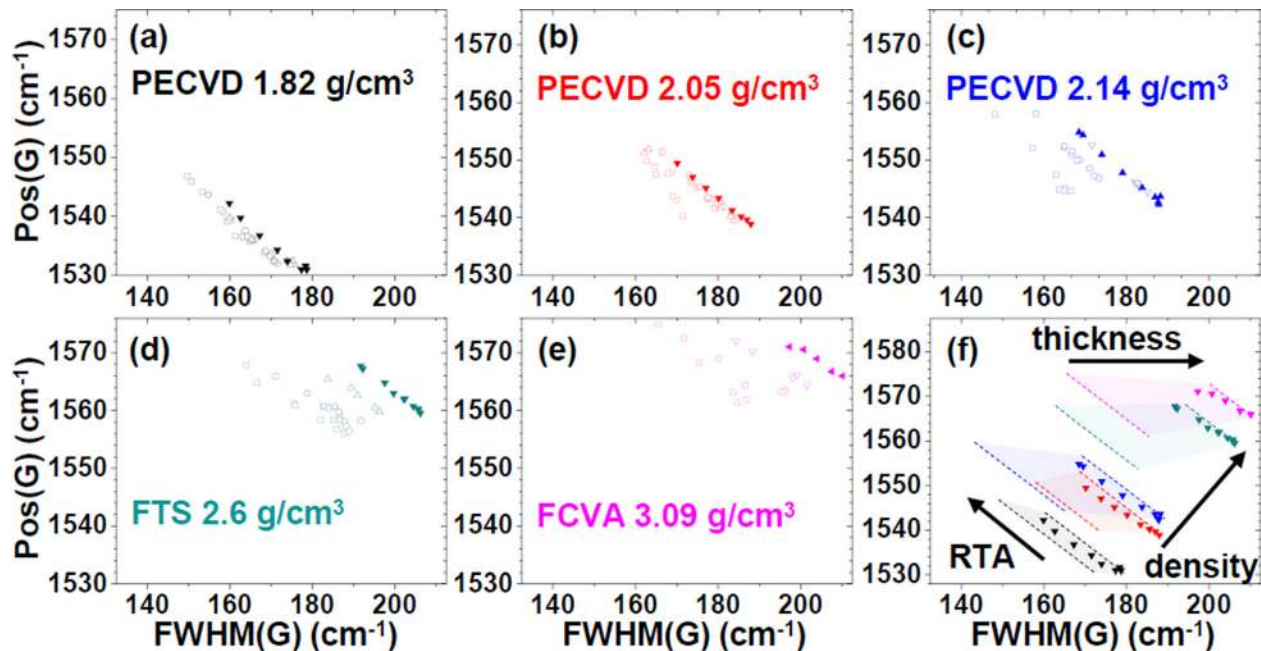

FIG. 2. Gaussian fitting of 514 nm Raman spectra of DLC:H. The charts of the variation of Pos(G) versus FWHM(G) permit distinguishing between films of different density and different thickness. The plots also allow monitoring the thermal evolution under 1 s RTA. For each series the data points follow the increasing annealing temperature (same as in Fig. 1). The first data point with lowest value of Pos(G) and highest value of FWHM(G) corresponds to the as-deposited film at 30 °C. The last point with highest values of Pos(G) and lowest value of FWHM(G) corresponds to 1 s RTA at around 650 °C. (a) to (e): open squares 20 Å, open circles 50 Å, open up triangles 100 Å, solid down triangles 200 Å. (f) Same data as in (a) to (e) but only data points for 200 Å thick films are plotted, the dashed lines and colored area are guides for the eyes and represent the spread of all the results in (a) to (e). Pos(G) and FWHM(G) values are reported in Raman shift expressed in wavenumber unit (cm⁻¹).
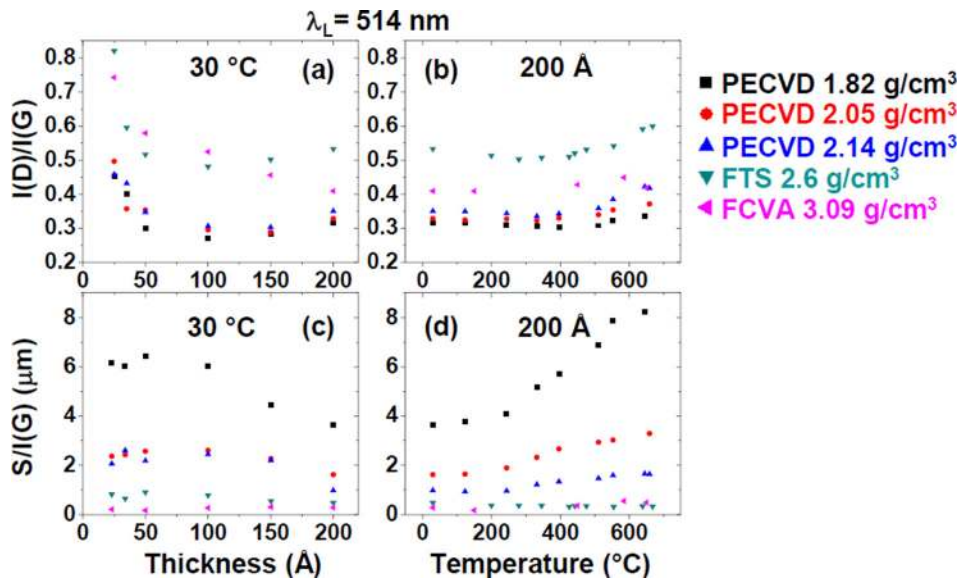
FIG. 3. Gaussian fitting of 514 nm Raman spectra of DLC:H. Variations of the I(D)/I(G) bands intensity ratio with thickness at 30 °C (a) and 1s RTA for 200 Å thick films (b). Variations of the S/I(G) PL slope over G intensity ratio with thickness at 30 °C (c) and 1s RTA for 200 Å thick films (d). Black squares, red circles, blue up triangles, cyan down triangles, and magenta left triangles stand for films with 1.82, 2.05, 2.14, 2.6, and 3.09 g/cm³, respectively.

how the sp^2 phase in DLC:H tends to cluster in the amorphous sp^3 matrix and in principle the clustering of the sp^2 phase is independent of the sp^3 content. In other words, since visible Raman spectroscopy is mainly a probe of different vibration modes of the sp^2 phase, two DLC:H films with different sp^3 fractions could exhibit the same visible Raman spectrum, intrinsically. This makes the determination of the carbon hybridization state on the basis of the I(D)/I(G) ratio unfeasible. Indeed, as reported in Fig. 3(a) the densest films, with the highest sp^3 fractions and the lowest hydrogen

contents (FTS and FCVA) exhibit higher I(D)/I(G) ratios than the more sp^2-bonded PECVD films.

V. MW RAMAN SPECTROSCOPY: sp³ CONTENT

As already discussed in Sec. IV, the I(D)/I(G) ratio measured at a particular visible laser wavelength λ_L does not represent the total amount of sp^2 bonding but rather the amount of sp^2-bonded clusters organized in rings that have a certain distribution of sizes and shapes which are Raman
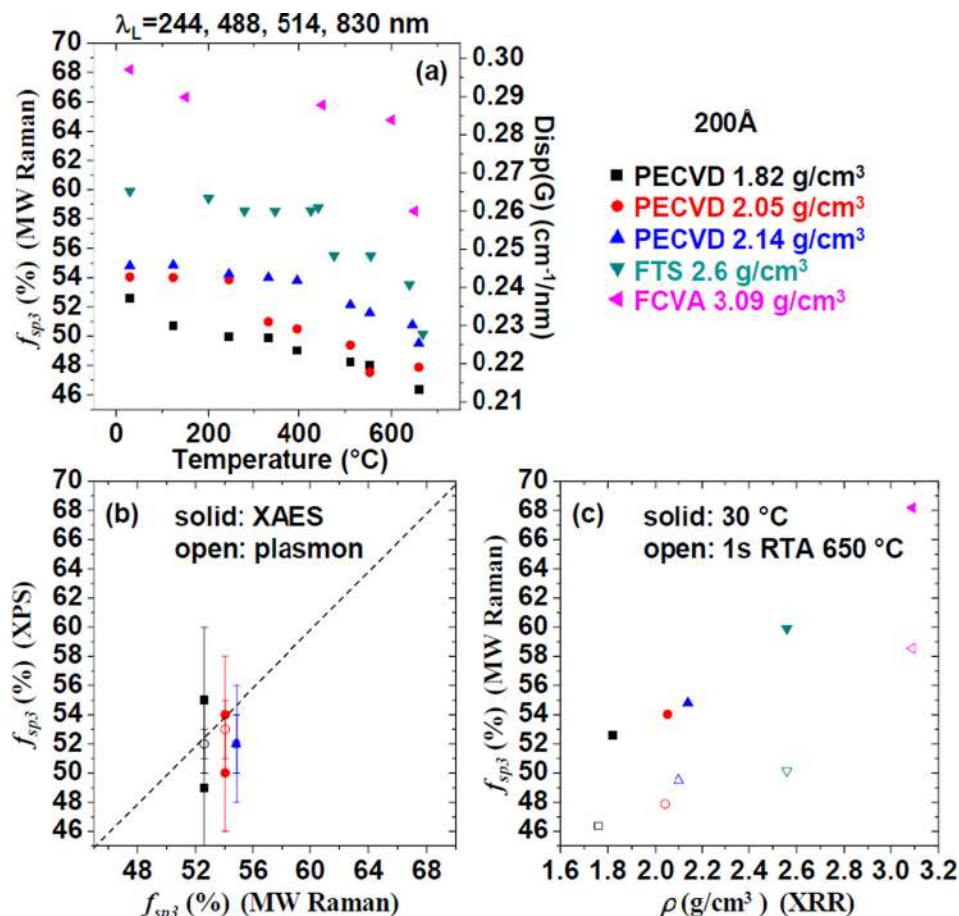

FIG. 4. Decrease of the sp^3 fraction f_{sp3} with increasing RTA temperature. (a) Disp(G), the dispersion of Pos(G) was measured by MW Raman spectroscopy (laser wavelengths λ_L of 244, 488, 514, and 830 nm). Each data point Disp(G) is the slope of the linear fit of the plot of Pos(G) versus λ_L and therefore expressed in cm^{-1}/nm units. Values in cm^{-1}/nm were converted into f_{sp3} percentage using the linear relationship in Ref. 54. (b) Comparison between f_{sp3} percentages measured by XPS and MW Raman in the case of PECVD films only. XAES and Plasmon data are represented by solid and open symbols, respectively. The median dashed line is a guide for the eye. (c) Correlation between sp^3 fraction f_{sp3} derived from MW Raman and mass density ρ measured by XRR before (solid symbols) and after 1s RTA at 650 °C (open symbols). Black squares, red circles, blue up triangles, cyan down triangles, and magenta left triangles represent films with 1.82, 2.05, 2.14, 2.6, and 3.09 g/cm³.

resonant at this particular laser wavelength λ_L.[1,35,54–68] By the same token, the use of the G band position Pos(G) alone (measured with one laser wavelength λ_L only) is not sufficient to completely describe and characterize an DLC:H film.[1,35,54–68] Each laser wavelength λ_L resonantly selects a narrow range of sp^2 clusters with a finite distribution of similar sizes and shapes (topological disorder). Higher excitation energies (UV, $\lambda_L = 244$ nm) can be more resonant with smaller clusters.[1,35,54–68] Indeed, visible Raman spectroscopy alone only probes a portion of the total sp^2 phase of a film. It measures the sp^2 portion that has a distribution of clusters where local band gaps are resonant at visible laser wavelengths λ_L. Utilizing multiple wavelengths from UV to visible to nIR (λ_L of 244, 488, 514, and 830 nm) allows for probing the entire distribution of sp^2 clusters in the film. Thus, only in the case of MW Raman spectroscopy, since the entire sp^2 phase of the films is measured, a correct calculation of the remaining corresponding sp^3 fraction f_{sp3} is possible. Therefore, it is necessary to measure the rate of change of Pos(G) with the excitation wavelength to distinguish between films with different sp^2 clustering[1,35,54–68] (Fig. 4(a)). We thus refer to the dispersion of Pos(G) versus λ_L as Disp(G) in units of cm^{-1}/nm. A lower value of Disp(G) corresponds to a greater degree of sp^2 clustering and a lower value of f_{sp3}. For instance, if two films have comparable Pos(G) in the visible, the film with lower Pos(G) measured in UV has higher sp^2 clustering.

For each type of film and for each annealing temperature, Disp(G) values were obtained by measuring the slope of the linear fit of the four Pos(G) data points obtained at λ_L of 244, 488, 514, and 830 nm. The standard deviation of Pos(G) is ± 1.5 cm^{-1} at 244, 488, and 514 nm and ± 9 cm^{-1} at 830 nm, respectively. Values of Disp(G) measured by MW Raman were then converted into values of f_{sp3} using the linear relationship $f_{sp3} = -0.07 + 2.5 \times$ Disp(G) (cm^{-1}/nm) ± 0.06 from Ref. 54 (Fig. 4(a)). It is noticed that this relationship between f_{sp3} and Disp(G) was derived for DLC films without hydrogen[54] and should in principle only be applied to the FCVA case. For the sake of comparison, we chose to apply this derivation to all DLC (FCVA) and DLC:H (PECVD, FTS) films. Using this measurement method, the Disp(G) and f_{sp3} values in Figure 4 are given with a $\pm 0.1\%$ statistical error. At lower temperature, sp^2 clustering does not occur necessarily with a change of sp^3 content. Therefore, converting Disp(G) into a f_{sp3} value is probably less accurate at lower temperature than at higher temperature where direct sp^3 to sp^2 conversion is more likely to occur. In Fig. 4(a), it can be remarked that the change in Disp(G) is very small at lower temperature and therefore that the effect of the inaccuracy in converting Disp(G) into a f_{sp3} value can be considered negligible. Higher f_{sp3} is usually correlated with higher ρ in the literature.[1] Similarly, we found that the as-deposited DLC:H films with the highest mass densities ρ are the ones with the highest sp^3 fractions f_{sp3} (Fig. 4(c)). For $\rho = 1.82$, 2.05, 2.14, 2.56, and 3.09 g/cm^3, the corresponding total C-C+C-H sp^3 contents f_{sp3} derived by MW Raman are 52.58 $\pm$ 0.1, 54.03 $\pm$ 0.1, 54.81 $\pm$ 0.1, 59.9 $\pm$ 0.1, and 68.18 $\pm$ 0.1%, respectively.

The f_{sp3} values derived from MW Raman results in the case of as-deposited PECVD films were compared to the

outcomes of XPS and XAES (Fig. 4(b)). The carbon hybridization state was obtained by measuring the intensity ratio of the components assigned to sp^2 and sp^3 carbon in the plasmon band near the C 1s XPS signal,[41,50] and the distance D between the most positive maximum and most negative minimum in the first derivative C KLL XAES spectrum[41,49–51] (D is approximately linearly proportional to the fraction of sp^2-hybridized carbon). As seen in Fig. 4(b), the results obtained by XPS (spectra not shown here[93]) are in agreement with MW Raman results within the error bars of the measurements. The values of the f_{sp3} fractions measured by plasmon and XAES are more spread out (uncertainty of the experimental results ranging from $\pm 1\%$ to $\pm 6\%$) than the values derived by MW Raman ($\pm 0.1\%$). In this study, the results obtained by the MW Raman method exhibit a higher resolution than those obtained by XPS. Only with MW Raman could we resolve quantitatively minute differences in f_{sp3} fractions between the PECVD films. We note that the XPS and XAES measurements probe the top 9.5 and 3.3 nm of the films, respectively; disagreement between MW Raman and the XPS and XAES values may be attributed to a distinct film structure in the near-surface region.

The results of Fig. 4(a) reveal that thermal annealing causes direct conversion of sp^3 into sp^2 bonded carbon for all types of films. The sp^3 fraction decreases monotonically with increasing annealing temperature. More precisely, the data in Fig. 4(a) indicate that up to approximately 400 °C all films exhibit a modest decrease of f_{sp3}, and the conversion of sp^3 into sp^2 accelerates above this temperature (one can observe a steeper slope in the curves of Fig. 4(a) above 400 °C). This latter observation is consistent with the model of Mangolini *et al.*[41] for the thermally induced structural evolution of DLC:H. In this model, the process for direct sp^3 to sp^2 conversion exhibits a higher activation energy than the other thermally induced processes (namely, the sp^2 clustering and hydrogen diffusion, as well as the resulting dangling bond passivation discussed in Sec. VII) and should therefore occur at higher annealing temperatures. After 1s RTA at 650 °C, the films actually retain more than 80% of their original sp^3 fraction ($f_{sp3} = 46.37$, 47.87, 49.51, 50.15, 58.53% for the films with $\rho = 1.82$, 2.05, 2.14, 2.56, and 3.09 g/cm^3, respectively). Moreover and most interestingly, we discovered that this loss of sp^3 hybridization is not accompanied by a loss of mass density. The correlation between f_{sp3} fraction derived from MW Raman and the mass density ρ measured by XRR before and after 1 s RTA at 650 °C is displayed in Fig. 4(c). It is quite striking that even though noticeable sp^3 hybridization loss and concomitant clustering of the sp^2 phase (as presented previously in Sec. IV) were measured after annealing, the films mass densities did not decrease.

The final configuration of the simulated DLC:H film with calculated mass density $\rho_{MD} = 2.15$ g/cm^3 and a thickness of $\sim$2.5 nm is shown in Fig. 5(a). Due to the energetic atom deposition process, the resulting film has a bi-layer structure consisting of a $\sim$2 nm uniform steady-growth film and a $\sim$0.5 nm surface layer. The hydrogen content through the DLC:H film is calculated to be $\sim$38 at. %. After simulated RTA, the MD model of the DLC:H film also reveals a decrease in the calculated sp^3 fraction f_{sp3-MD} with annealing
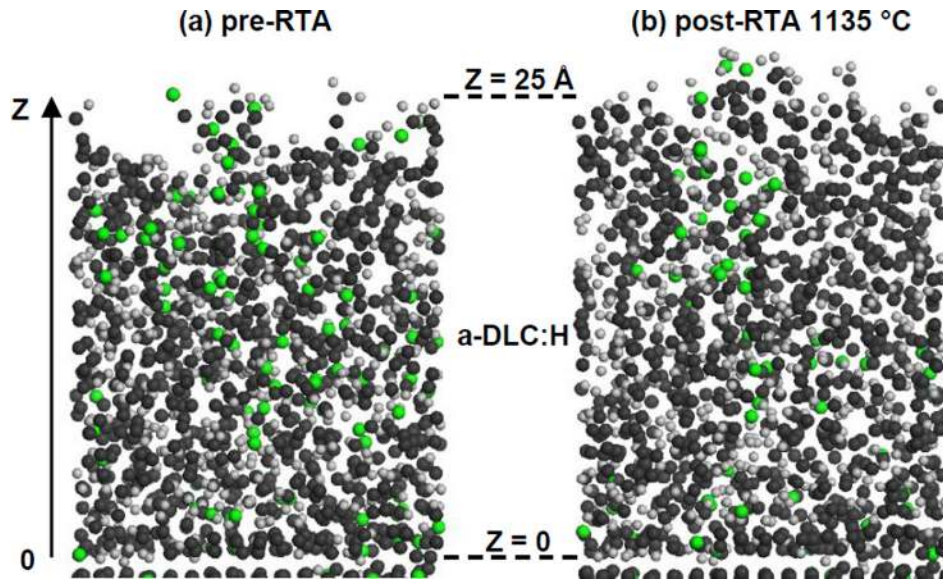
FIG. 5. Molecular dynamics models of DLC:H film on diamond (100). (a) Pre-RTA: the deepest 20 Å layers of the DLC:H film have a mass density ρ_{MD} of 2.15 g/cm^3 and a hydrogen content of 38%. (b) Post RTA treatment at 1135 °C. The depiction includes carbon atoms with dangling bonds (green), the remaining carbon atoms (gray), and the hydrogen atoms (white). The Z coordinate of the film is defined by Z = 0 at the diamond substrate and Z = 25 Å at the pre-RTA film's surface. The diamond substrate is not shown. During RTA simulation, the bottom layer of the diamond substrate is fixed; the middle 4 Å thick layer of atoms is constrained by the Berendsen thermostat at room temperature; and the top 6 Å thick layer of atoms forming the substrate for DLC:H growth are constraint-free.

temperature as reported in Table II. Here, $f_{sp3\text{-}MD}$ is defined based on the atom coordination number with a cutoff radius of 2 Å. Although the sp^3 fraction is underestimated by the REBO potential due to the short cutoff distance in the potential functions, the relative sp^3 to sp^2 conversion trend is in good agreement with the Raman data. At higher annealing temperature, the conversion is accelerated almost exponentially. Similarly to the XRR results, the density of the model film is mostly stable with increasing annealing temperature (Table II). This finding not only supports the idea presented in the Robertson model[1] that the sp^2 and sp^3 phases can evolve separately and in a different fashion whether the evolution follows the amorphization or crystallization direction (see Sec. VI) but also that the mass density does not depend exclusively and strictly on the sp^3 fraction. Our study clearly reveals that two films with different hybridization and microstructure can have the same mass density. Indeed, to be able to completely characterize a film, one needs more information than only f_{sp3}, for instance knowledge of a film's post-growth treatment should also be accounted for (i.e., as-deposited film or a post-annealed film).

We present in the next section that (a) the description of the disorder in the sp^2 phase also has to be taken into account, and (b) to be able to characterize films with different densities one needs more information than the sp^3

TABLE II. Calculated sp^3 fraction $f_{sp3\text{-}MD}$ and calculated mass density ρ_{MD} at the equilibrium state after annealing versus peak temperature during numerical experiments. The standard deviations (noted as standard deviation) are given in the adjacent respective columns. The sp^3 fraction decreases significantly when peak temperature is higher than 744 °C, but the density of the bulk film is relatively stable.

1s RTA (°C)	$f_{sp3\text{-}MD}$ (%)	Standard deviation	ρ_{MD} (g/cm^3)	Standard deviation
27	30.05	0.478	2.131	0.021
317	29.7	0.454	2.14	0.026
569	28.75	0.388	2.118	0.029
744	26.78	0.349	2.088	0.022
1134	22.15	0.355	1.987	0.031

content only or more than one Raman parameter. In Sec. VI, we describe a new analysis method, namely the variation of Pos(G) versus FWHM(G), and demonstrate that this method allows for a complete characterization of a film: its growth history (its density and the type of deposition method it was prepared with), its thermal evolution (at what temperature it was annealed to), and even its thickness.

VI. A NEW ANALYSIS METHOD OF RAMAN SPECTRA: POS(G) VERSUS FWHM(G)

In Sec. V, we have shown that the use of the G band position Pos(G) alone (topological disorder measured with one laser wavelength λ_L only) or the value of the sp^3 fraction f_{sp3} alone is not sufficient to completely describe and characterize structural variations between different types of DLC:H films. The reason for this is that sp^2 clusters also possess a distribution of bond lengths and angles (structural disorder) which corresponds to a unique G band full width at half maximum FWHM(G) for each excitation wavelength. If clusters are perfectly organized without defects and strain, then FWHM(G) becomes negligible.[1] In contrast, a higher value of FWHM(G) reflects a wider distribution of bond lengths and bond angles for clusters with roughly a similar size and probed by the same unique excitation wavelength.[1] Indeed, one Raman parameter alone, I(D)/I(G) or Pos(G) or FWHM(G) cannot be used to fully characterize an DLC:H film. In this article, we report in the case of $\lambda_L = 514$ nm that it is possible to differentiate between films with different mass density or thickness and between as-deposited and post-annealed films by plotting the evolution of Pos(G) versus FWHM(G). A chart for each of the five types of DLC:H films having different density is displayed in Fig. 2. The evolution of Pos(G) versus FWHM(G) under 1 s RTA in air is plotted for 25, 50, 100, and 200 Å thick films. All charts in Fig. 2 are plotted on the same scale to allow direct comparison between them. To emphasize the trends in thickness, density, and RTA, the data in Figs. 2(a)–2(e) corresponding to 200 Å thick films are reported on the same chart in Fig. 2(f). The spread of the data with thickness (as measured in Figs. 2(a)–2(e)) is indicated by the shaded areas and the dashed lines.

Fig. 2 shows that (a) denser films have higher values of both Pos(G) and FWHM(G), (b) 1 s RTA between 30 and 659 °C after deposition leads to higher Pos(G) and lower FWHM(G) values, and (c) FWHM(G) increases with thickness with a larger spread of values for denser films. These results are in excellent agreement with the hysteresis model by Ferrari,[1,35,64,65] i.e., the evolution of the Raman parameters can be different if one follows the evolution of the films in the amorphization direction (for example by changing the deposition method, from purely sp^2 graphite to purely sp^3 tetrahedral amorphous carbon) or in the opposite crystallization direction (for example, by post-annealing DLC:H). In other words, Pos(G) versus FWHM(G) charts in Fig. 2 show that if two films have the same Pos(G), the film with the lower FWHM(G) is thinner or less dense or has been post-annealed after deposition.

Based on correlations drawn in the literature,[1] an empirical conclusion would be that loss of sp^3 content by annealing readily translates into reduced mass density of DLC:H films. We have reported in Sec. V that it is not necessarily the case and that densities measured by XRR on all our 200 Å thick DLC:H films are actually not changed by 1 s RTA at 659 °C (Fig. 4(c) and Table I). In the plots of Fig. 2, it is remarkable that for each type of film (PECVD 60, 120, and 180 V, FTS, and FCVA) and each thickness (25, 50, 100, and 200 Å), the evolution of Pos(G) versus FWHM(G) with increasing annealing temperature follows a straight line. In particular, we compare in Fig. 2(f) this linear correlation between Pos(G) versus FWHM(G) for all 200 Å thick films. Each set of data corresponds to one line, one for each type of film with a constant density for all annealing temperatures. Lines of data are arranged in the chart without overlap with each other in order of increasing density toward increasing Pos(G) and FWHM(G). Therefore, values of Pos(G) and FWHM(G) completely describe an DLC:H. In the plots of Fig. 2, a pair of Pos(G) and FWHM(G) is sufficient to determine the corresponding deposition method, density, thickness, and annealing temperature for each film.

It is clear that the evolution of Pos(G) versus FWHM(G) with RTA is similar for all types of DLC:H, but the dependence and evolution with thickness is more pronounced for denser films. In Fig. 2, the data for all thicknesses overlap in the case of PECVD 1.82 g/cm^3, but are up-shifted in FWHM(G) for increasing thickness and increasing density. The spread in FWHM(G) is the largest for the densest films, namely FTS 2.6 g/cm^3 and FCVA 3.09 g/cm^3 which are also the most sp^3-rich, as measured by MW Raman (Fig. 4). These results suggest that (a) thicker films of FTS and FCVA exhibit different clustering of the carbon sp^2 phase than thinner films, and (b) that the surface of FTS and FCVA films is more sp^2 than the deeper layers of the films. This latter conclusion is supported by the comparison of the Raman results with the outcomes of XPS, XAES, and near-edge X-ray absorption fine structure (NEXAFS) spectroscopy analyses (the complete X-ray study is not shown here and will be the subject of another publication[93]). The higher fraction of sp^2-bonded carbon measured by XAES (whose information depth is 3.3 nm) compared to the fraction of sp^2-bonded carbon determined by XPS (whose information depth is up to

9.5 nm) clearly suggests the presence of an outermost layer on FTS and FCVA films that is richer in threefold-coordinated carbon atoms.[93]

VII. PHOTOLUMINESCENCE MODEL AND DANGLING BONDS PASSIVATION

As previously mentioned, the π states of the sp^2 phase organized in clusters form the conduction and valence band edges in DLC:H.[1,38–40,69–73] The distribution of size and shape of the disordered π clusters is the cause for a spatially inhomogeneous band gap with highly disordered and localized band edges.[1,38–40,69–73] The presence of disorder in the clusters generates band tail states that extend deep in the gap.[1,38–40,69–73] Under laser irradiation, PL can take place between localized conduction and valence bands tail states (Figs. 1(c) and 1(d)). For instance, it has been proposed[1,38–40,69–73] that disorder induced by distorted aromatic rings produces localized states due to the modification of the π molecular orbitals. Transitions between these modified molecular orbitals can lead to PL bands at different energies. The PL model of DLC:H is somewhat similar to the case of a-Si:H:[94] it starts with the creation of an electron-hole pair by a light scattering event, then its thermalization via phonons inside the valence and conduction bands, then its trapping in band tail states, followed by its radiative recombination. The particularity of the DLC:H case arises from the fact that the band tails are very wide and overlap with a high density of mid-gap defect states.[1,38–40,69–73] These defect states are mainly due to dangling bonds or topological disorder such as rings with an odd number of atoms. These states form non-radiative centers that compete with PL centers for electron-hole pair recombination. Passivation of dangling bonds by hydrogen and by clustering of weekly bonded sp^2 clusters reduces the number of available non-radiative recombination centers and thus induces an increase in PL activity.[1,38–40,69–73] Therefore, PL spectroscopy is an indirect way of quantifying the hydrogen content of as-deposited DLC:H films.[1,38–40,69–73] As seen in Figs. 1(c) and 1(d), the PL signal decreases for denser films. This result is in excellent agreement with HFS measurements in Table I: denser as-deposited films (RT) contain less hydrogen. It also suggests that the carbon network of denser films has a higher amount of non-radiative centers, most probably dangling bonds.

If a PL filter is not available to obtain the whole PL spectrum experimentally, the hydrogen content can also be estimated by taking the ratio of the slope S of the PL background below the first order Raman spectrum to the intensity of the G band.[69] The quantity S/I(G) expressed in micrometer in Figs. 3(c) and 3(d) is negligible for FTS and FCVA in comparison with PECVD. The overall higher value S/I(G) for PECVD can be explained by the higher hydrogen content f_H (Table I) of these films which renders them more polymeric than FTS and FCVA films. The presence of hydrogen limits the formation of dangling bonds (non-radiative recombination centers), as well as the formation of clusters of aromatic rings (as evidenced by the low I(D)/I(G) ratio of these films). Whereas all three PECVD films have a similar f_H

around 32%, it is noticeable that the S/I(G) of the less dense PECVD film ($\rho = 1.82$ g/cm^3, $f_{sp3} = 52.58\%$) is significantly higher than all the other films and also exhibits a more pronounced variation with thickness and with RTA. The precise origin for this behavior cannot be completely understood at that point, but we suggest that the enhanced PL activity of these films is probably due to a reduced presence of dangling bonds and a larger fraction of the sp^2 phase organized in chains or in rings that are disordered, distorted, or comprised of closed chains such that the bonds are not fully delocalized on the rings.[1,38–40,69–73]

Annealing of DLC:H can induce changes in the density of states, especially at the band tail edges, by promoting better passivation of dangling bonds due to hydrogen diffusion in the film and by re-clustering of weekly bonded sp^2 clusters.[1,38–40,69–73] These changes in band edges and gap states control the magnitude of the PL activity. Fig. 6 shows the evolution of dangling bond density with annealing temperature for the MD-simulated film $\rho_{MD} = 2.15$ g/cm^3. The dangling bond density appears to decrease linearly for the range of peak temperatures investigated. The linear fit in Fig. 6 has a slope of -0.0035×10^{21} cm^{-3} °C^{-1} and intercept of 8.07×10^{21} cm^{-3}. The large increase in the PL intensity of the PECVD film with $\rho = 2.14$ g/cm^3 at 659 °C in Figure 1(b) can be correlated to around a 25% decrease in the calculated dangling bond density for the same peak temperature in Fig. 6.

Furthermore, Fig. 5 depicts the location of the dangling bonds in the simulated film before and after RTA, where carbon atoms with dangling bonds are labeled in green. The corresponding variation of the number of dangling bonds as a function of the Z coordinate is given in Fig. 7. In Figs. 5 and 7, the total number of dangling bonds is 100 pre-RTA and 67 post-RTA at 1135 °C. This analysis of the simulated DLC:H networks reveals that prior to RTA (Fig. 7(a)), the dangling bond density is higher near the substrate-film interface (Z = 0 Å) and just below the topical layer (Z = 25 Å). After RTA treatment at 1135 °C (Fig. 7(b)), most of the dangling bonds in the region just below the surface layer of the film have been passivated.

FIG. 7. The distribution of dangling bonds along the Z coordinate of the corresponding simulated films in Fig. 5. The coordinate is defined by Z = 0 at the diamond substrate and Z = 25 Å at the pre-RTA film's surface. (a) Pre-RTA and (b) post-RTA treatment at 1135 °C.

The bond order analysis demonstrates a significant difference between the stability of the C-to-C and the C-to-H bonds. The number of C bonds with bond order of 2 (double bonds in Fig. 8(a)) consistently increases during RTA treatment, corresponding to an increase in sp^2 fraction within the film. However, the C-H bonds remain relatively stable, and the loss of hydrogen is indeed minor during RTA (Fig. 8(b)). Moreover, HFS measurements confirmed that little hydrogen is lost during 1 s RTA at 650 °C. H content of films with ρ of 1.82, 2.05, 2.14, 2.56, and 3.09 g/cm^3 only decrease from $f_H = 32.5$, 32, 30.5, 5.8, and less than 0.5% down to 24.7, 27.5, 28, 5.5 and less than 0.5%, respectively (Table I).

Once again, the reduction of defect density and the retention of most of the hydrogen both as calculated by MD are in good agreement with the increase in PL activity in Fig. 1(b).[1,38–40,69–73] Thus, we conclude from MD simulations that the observed passivation of dangling bonds is primarily driven by sp^2 clustering and C reorganization rather than by hydrogen diffusion.
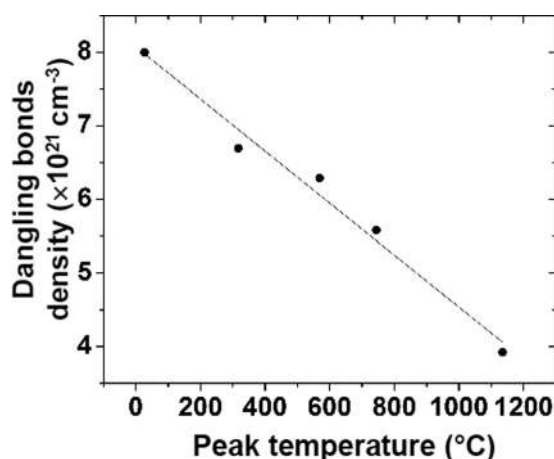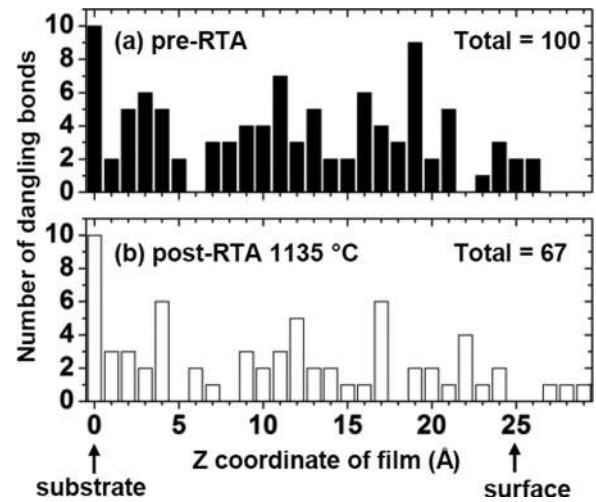

FIG. 6. Dangling bonds density as a function of RTA peak temperature for the MD simulated film. The line is a linear fit (slope -0.0035×10^{21} cm^{-3} °C^{-1}, intercept 8.07×10^{21} cm^{-3}).
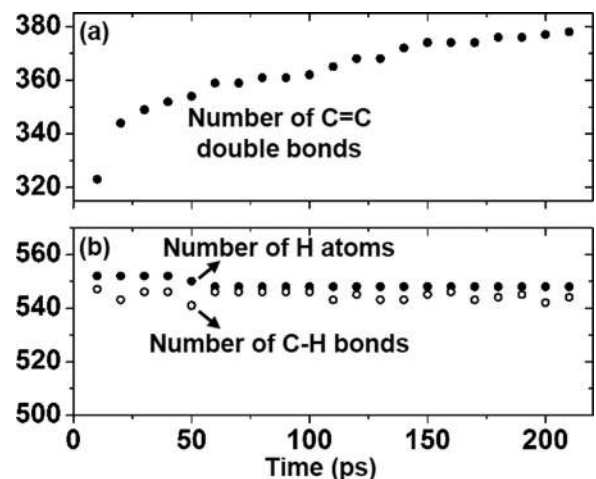

FIG. 8. Time evolution of the number of (a) C double bonds (order 2) and (b) C-H bonds (open circles) and H atoms (solid circles) observed in the simulated films during exposure to a peak RTA temperature of 1135 °C.

VIII. CONCLUSIONS AND PERSPECTIVES

We have shown that more than one Raman parameter is necessary to completely describe minute structural differences between thin DLC:H films grown by PECVD, FTS, and FCVA and treated by RTA. The difficulty in interpreting Raman spectra stems from the fact that sp^2 clusters possess complex structural and topological disorder that lead locally to the formation of different band gaps that are more or less resonant with different Raman laser wavelengths. To overcome this difficulty, we used a new analysis method that consists of plotting the variation of Pos(G) (structural disorder) versus FWHM(G) (topological disorder) and demonstrated that it permits one to distinguish unequivocally between films prepared with different density, thickness, and RTA treatment. Indeed, denser films exhibit larger values of both Pos(G) and FWHM(G), thicker films larger values of FWHM(G), and RTA treated films larger values of Pos(G) and smaller values of FWHM(G). We have reported that the evolution of the sp^2 and sp^3 phases in DLC:H can be independent and governed by the treatment of the film post-deposition. More precisely, by performing XRR, XPS, HFS, and MW Raman we found that films treated by RTA can retain their mass density and hydrogen content while experiencing a loss of sp^3 fraction. In the 180 V PECVD case, MD was successfully used to model the amorphous network and simulate its evolution during RTA. MD analysis was in excellent agreement with experimental spectroscopic results and allowed for understanding the process which creates the increase in PL activity and concomitant passivation of non-radiative recombination centers during RTA. It was concluded that dangling bonds passivation is primarily the result thermally-induced sp^2 clustering rather than hydrogen diffusion in the film.

To complete the current study, more experimental and simulation work will be needed to understand the exact processes leading to PL activity. The identification of the local sites in the network responsible for the appearance of radiative centers in the gap (tail states and/or defects states) is still missing. Also, more X-ray spectroscopy should be conducted to precisely assess the non-uniform cross-sectional structure of thin films, especially to measure the difference in sp^3 and sp^2 fractions between the surface and the bulk film. In order to predict the properties and performance of simulated carbon amorphous networks, we also hope that future developments of *ab-initio* methods will allow for the calculation of resonant Raman spectra.

[1]J. Robertson, Mater. Sci. Eng., R **37**, 129 (2002).
[2]K. Bewilogua and D. Hofmann, Surf. Coat. Technol. **242**, 214 (2014).
[3]A. Grill, Diamond Relat. Mater. **8**, 428 (1999).
[4]C. A. Charitidis, Int. J. Refract. Met. Hard Mater. **28**, 51 (2010).
[5]J. Robertson, Tribol. Int. **36**, 405 (2003).
[6]J. Robertson, Thin Solid Films **383**, 81 (2001).
[7]A. C. Ferrari, Surf. Coat. Technol. **180–181**, 190 (2004).
[8]C. Casiraghi, J. Robertson, and A. C. Ferrari, Mater. Today **10**, 44 (2007).
[9]S. Pirzada, J. J. Liu, F. Li, B. Demczyk, and D. Spaulding, J. Appl. Phys. **91**, 7562 (2002).
[10]K. J. Grannen, X. Ma, R. Thangaraj, J. Gui, and G. C. Rauch, IEEE Trans. Magn. **36**, 120 (2000).
[11]B. Marchon, T. Pitchford, Y.-T. Hsia, and S. Gangopadhyay, Adv. Tribol. **2013**, 521086.
[12]B. Marchon and T. Olson, IEEE Trans. Magn. **45**, 3608 (2009).
[13]N. Wang and K. Komvopoulos, J. Mater. Res. **28**, 2124 (2013).
[14]M. P. Siegal, P. N. Provencio, D. R. Tallant, R. L. Simpson, B. Kleinsorge, and W. I. Milne, Appl. Phys. Lett. **76**, 2047 (2000).
[15]C. A. Davis, G. A. J. Amaratunga, and K. M. Knowles, Phys. Rev. Lett. **80**, 3280 (1998).
[16]C. A. Davis, K. M. Knowles, and G. A. J. Amaratunga, Surf. Coat. Technol. **76–77**, 316 (1995).
[17]E. Riedo, F. Comin, J. Chevrier, F. Schmithusen, S. Decossas, and M. Sancrotti, Surf. Coat. Technol. **125**, 124 (2000).
[18]Y. Lifshitz, S. R. Kasi, J. W. Rabalais, and W. Eckstein, Phys. Rev. B **41**, 10468 (1990).
[19]M. H. Kryder, E. C. Gage, T. W. Mcdaniel, W. A. Challener, R. E. Rottmayer, G. Ju, Y. T. Hsia, and M. F. Erden, Proc. IEEE **96**, 1810 (2008).
[20]W. A. Challener, C. Peng, A. V. Itagi, D. Karns, W. Peng, Y. Peng1, X. Yang, X. Zhu, N. J. Gokemeijer, Y.-T. Hsia, G. Ju, R. E. Rottmayer, M. A. Seigler, and E. C. Gage, Nature Photon. **3**, 220 (2009).
[21]B. C. Stipe, T. C. Strand, C. C. Poon, H. Balamane, T. D. Boone, J. A. Katine, J.-L. Li, V. Rawat, H. Nemoto, A. Hirotsune, O. Hellwig, R. Ruiz, E. Dobisz, D. S. Kercher, N. Robertson, T. R. Albrecht, and B. D. Terris, Nature Photon. **4**, 484 (2010).
[22]S. Xiong, J. Kim, Y. Wang, X. Zhang, and D. Bogy, J. Appl. Phys. **115**, 17B702 (2014).
[23]P. M. Jones, J. Ahner, C. L. Platt, H. Tang, and J. Hohlfeld, IEEE Trans. Magn. **50**, 3300704 (2014).
[24]B. Marchon, X.-C. Guo, B. K. Pathem, F. Rose, Q. Dai, N. Feliss, E. Schreck, J. Reiner, O. Mosendz, K. Takano, H. Do, J. Burns, and Yoko Saito, IEEE Trans. Magn. **50**, 3300607 (2014).
[25]S. Xiong and D. B. Bogy, IEEE Trans. Magn. **50**, 1 (2014).
[26]N. Tagawa, H. Tani, and K. Ueda, Tribol. Lett. **44**, 81 (2011).
[27]Y. S. Ma, Y. J. Man, M. Shakerzadeh, H. L. Seet, R. Ji, R. Y. Zheng, H. J. Chung, X. Y. Chen, J. F. Hu, T. Yamamoto, and R. Hempstead, Tribol. Lett. **53**, 303 (2014).
[28]M. Shakerzadeh, Y. Ma, M. Tadayon, R. Ji, H. S. Tan, and B. K. Tay, Surf Coat. Technol. **236**, 207 (2013).
[29]N. Wang, K. Komvopoulos, F. Rose, and B. Marchon, J. Appl. Phys. **113**, 083517 (2013).
[30]B. K. Pathem, X.-C. Guo, F. Rose, N. Wang, K. Komvopoulos, E. Schreck, and B. Marchon, IEEE Trans. Magn. **49**, 3721 (2013).
[31]C. Hopf, T. Angot, E. Aréou, T. Dürbeck, W. Jacob, C. Martin, C. Pardanaud, P. Roubin, and T. Schwarz-Sellinger, Diamond Relat. Mater. **37**, 97 (2013).
[32]Y. S. Park and B. Hong, J. Non-Cryst. Solids **354**, 3980 (2008).
[33]S. Takabayashi, K. Okamoto, H. Sakaue, T. Takahagi, K. Shimada, and T. Nakatani, J. Appl. Phys. **104**, 043512 (2008).
[34]H. Li, T. Xu, C. Wang, J. Chen, H. Zhou, and H. Liu, Thin Solid Films **515**, 2153 (2006).
[35]A. C. Ferrari and J. Robertson, Phys. Rev. B **64**, 075414 (2001).
[36]A. Ilie, A. C. Ferrari, T. Yagi, and J. Robertson, Appl. Phys. Lett. **76**, 2627 (2000).
[37]A. C. Ferrari, B. Kleinsorge, N. A. Morrison, A. Hart, V. Stolojan, and J. Robertson, J. Appl. Phys. **85**, 7191 (1999).
[38]N. M. J. Conway, A. C. Ferrari, A. J. Flewitt, J. Robertson, W. I. Milne, A. Tagliaferro, and W. Beyer, Diamond Relat. Mater. **9**, 765 (2000).

[39]N. M. J. Conway, A. Ilie, J. Robertson, W. I. Milne, and A. Tagliaferro, Appl. Phys. Lett. **73**, 2456 (1998).

[40]Y.-Z. Yoo and J.-H. Song, Trans. Electr. Electron. Mater. **12**, 89 (2011).

[41]F. Mangolini, F. Rose, J. Hilbert, and R. W. Carpick, Appl. Phys. Lett. **103**, 161605 (2013).

[42]J. P. Sullivan, T. Friedmann, and A. Baca, J. Electron. Mater. **26**, 1021 (1997).

[43]A. C. Ferrari, S. Rodil, J. Robertson, and W. Milne, Diamond Relat. Mater. **11**, 994 (2002).

[44]D. S. Grierson, A. V. Sumant, A. R. Konicek, T. A. Friedmann, J. P. Sullivan, and R. W. Carpick, J. Appl. Phys. **107**, 033523 (2010).

[45]G. Jungnickel, Th. Frauenheim, D. Porezag, P. Blaudeck, U. Stephan, and R. J. Newport, Phys. Rev. B **50**, 6709 (1994).

[46]H. U. Jäger and K. Albe, J. Appl. Phys. **88**, 1129 (2000).

[47]N. Marks, Diamond Relat. Mater. **14**, 1223 (2005).

[48]N. Marks, J. Phys: Condens. Matter. **14**, 2901 (2002).

[49]S. Kaciulis, Surf. Interface Anal. **44**, 1155 (2012).

[50]A. Mezzi and S. Kaciulis, Surf. Interface Anal. **42**, 1082 (2010).

[51]P. K. Chu and L. Li, Mater. Chem. Phys. **96**, 253 (2006).

[52]A. C. Ferrari, A. Libassi, B. K. Tanner, V. Stolojan, J. Yuan, L. M. Brown, S. E. Rodil, B. Kleinsorge, and J. Robertson, Phys. Rev. B **62**, 11089 (2000).

[53]C. Mathew Mate, B. K. Yen, D. C. Miller, M. F. Toney, M. Scarpulla, and J. E. Frommer, IEEE Trans. Magn. **36**, 110 (2000).

[54]W. G. Cui *et al.*, Surf. Coat. Technol. **205**, 1995 (2010).

[55]M. Ramsteiner and J. Wagner, Appl. Phys. Lett. **51**, 1355 (1987).

[56]K. W. R. Gilkes, H. S. Sands, D. N. Batchelder, J. Robertson, and W. I. Milne, Appl. Phys. Lett. **70**, 1980 (1997).

[57]K. W. R. Gilkes, S. Prawera, K. W. Nugent, J. Robertson, H. S. Sands, Y. Lifshitz, and X. Shi, J. Appl. Phys. **87**, 7283 (2000).

[58]V. Paillard, Europhys. Lett. **54**, 194 (2001).

[59]F.-X. Liu, K.-L. Yao, and Z.-L. Liu, Appl. Surf. Sci. **253**, 6957 (2007).

[60]F.-X. Liu, K.-L. Yao, and Z.-L. Liu, Diamond Relat. Mater. **16**, 1746 (2007).

[61]F.-X. Liu and Z.-L. Wang, Surf. Coat. Technol. **203**, 1829 (2009).

[62]M. H. Oliveira, Jr., G. A. Viana, M. M. de Lima, Jr., A. Cros, A. Cantarero, and F. C. Marques, J. Appl. Phys. **108**, 123525 (2010).

[63]J. Wasyluk, T. S. Perova, D. W. M. Lau, M. B. Taylor, D. G. McCulloch, and J. Stopford, Diamond Relat. Mater. **19**, 514 (2010).

[64]A. C. Ferrari and J. Robertson, Phys. Rev. B **61**, 14095 (2000).

[65]C. Casiraghi, A. C. Ferrari, and J. Robertson, Phys. Rev. B **72**, 085401 (2005).

[66]S. Piscanec, F. Mauri, A. C. Ferrari, M. Lazzeri, and J. Robertson, Diamond Relat. Mater. **14**, 1078 (2005).

[67]C. Casiraghi, Diamond Relat. Mater. **20**, 120 (2011).

[68]E. F. Motta, G. A. Viana, D. S. Silva, A. D. S. Côrtes, F. L. Freire, Jr., and F. C. Marques, J. Vac. Sci. Technol. A **31**, 021502 (2013).

[69]B. Marchon, J. Gui, K. Grannen, G. C. Rauch, J. W. Ager III, S. R. P. Silva, and J. Roberston, IEEE Trans. Magn. **33**, 3148 (1997).

[70]J. Robertson, Phys. Rev. B **53**, 16302 (1996).

[71]J. Robertson, Diamond Relat. Mater. **5**, 457 (1996).

[72]Rusli, J. Robertson, and G. A. J. Amaratunga, J. Appl. Phys. **80**, 2998 (1996).

[73]G. Adamopoulos, J. Robertson, N. A. Morrison, and C. Godet, J. Appl. Phys. **96**, 6348 (2004).

[74]S. Butterworth, "Experimental wireless and the wireless engineer," Wireless Eng. **7**, 536 (1930).

[75]H. F. M. Boelensa, R. J. Dijkstrab, P. H. C. Eilersc, F. Fitzpatrickd, and J. A. Westerhuisa, J. Chromatogr. A **1057**, 21 (2004).

[76]K. Levenberg, Quart. Appl. Math. **2**, 164 (1944).

[77]D. Marquardt, J. Appl. Math. **11**, 431 (1963).

[78]D. W. Brenner, Phys. Rev. B **42**, 9458 (1990).

[79]D. W. Brenner, Phys. Rev. B **46**, 1948 (1992).

[80]D. W. Brenner, O. A. Shenderova, J. A. Harrison, S. J. Stuart, B. Ni, and S. B. Sinnott, J. Phys: Condens. Matter. **14**, 783 (2002).

[81]S. J. Stuart, A. B. Tutein, and J. A. Harrison, J. Chem. Phys. **112**, 6472 (2000).

[82]S. Plimpton, J. Comput. Phys. **117**, 1 (1995).

[83]H. J. C. Berendsen, J. P. M. Postma, W. F. van Gunsteren, A. DiNola, and J. R. Haak, J. Chem. Phys. **81**, 3684 (1984).

[84]T. Ma, Y.-Z. Hu, H. Wang, and X. Li, Phys. Rev. B **75**, 035425 (2007).

[85]N. Marks, Phys. Rev. B **56**, 2441 (1997).

[86]Materials Studio v6.1, Accelrys Software Inc., San Diego, CA, USA.

[87]A. C. Ferrari, Solid State Commun. **143**, 47 (2007).

[88]A. C. Ferrari and J. Robertson, Phil. Trans. R. Soc. London, Ser. A **362**, 2477 (2004).

[89]S. Pisana, T. C. Casiraghi, A. C. Ferrari, and J. Robertson, Diamond Relat. Mater. **15**, 898 (2006).

[90]W. H. Weber and R. Merlin, *Raman Scattering in Materials Science* (Springer-Verlag Berlin, Heidelberg, 2000).

[91]C. Thomsen and S. Reich, Phys. Rev. Lett. **85**, 5214 (2000).

[92]S. Reich and C. Thomsen, Philos. Trans. R. Soc. London, Ser. A **362**, 2271 (2004).

[93]F. Mangolini, J. B. McClimon, F. Rose, and R. W. Carpick, "Measuring Schmutz: Accounting for nanometer-thick adventitious carbon contamination in x-Ray absorption spectra of carbon-based materials," Analy. Chem. (submitted).

[94]S. Liedtke, K. Jahn, F. Finger, and W. Fuhs, J. Non-Cryst. Solids **97–98**, 1083 (1987).